Experiments in Fluids 11, 77–86 (1991)

Experiments in Fluids

Digital particle image thermometry: The method and implementation

D. Dabiri and **M. Gharib**

Department of Applied Mechanics and Engineering Sciences, R-011, University of California, San Diego, La Jolla, CA 92093, USA

Abstract. A computerized flow visualization technique capable of automatically quantifying the temperature field in a two-dimensional cross section of a flow field is described. The temperature sensors used are fast-response temperature-sensitive micro-encapsulated liquid crystal particles. Illuminating the flow by a thin sheet of white light, the reflected colors from the liquid-crystal particles were captured through a 3-chip video color camera and stored onto a videotape for subsequent data processing. The temperature field was obtained through an automatic color-temperature calibration scheme in *HSI* rather than *RGB* space, thus allowing for data processing of approximately one-third the time of *RGB* processing. The technique is finally applied to the study of a heated vortex-ring and some preliminary results are discussed.

1 Introduction

1.1 Background

While the velocity and vorticity fields are the primary quantities that characterize a given flow field, it is the information regarding distribution of scalar fields such as temperature and concentration that are sought in order to evaluate performance of various fluid mechanical systems such as mixers and heat exchangers. In this regard simultaneous evaluation of vector and scalar fields (e.g. vorticity and temperature) is extremely important.

In recent years the advent of particle tracking or image velocimetry has made it possible to obtain high resolution global velocity and vorticity fields. In the meantime, laser induced fluorescence technique has been used to obtain high resolution measurement of concentration in gas or liquid flows. However, the techniques for measuring temperature, a more important scalar field, have shown less progress since they were mainly limited to single point thermocouple measurements. The more global techniques such as IR imagery suffer from poor resolution. In this respect liquid crystal particles can offer better resolution and dynamic range. However, their wide application has been limited due to technical problems associated with measuring color accurately.

It is the purpose of this paper to present the concept of digital particle image thermometry which is based on extracting the temperature field from the color response of the suspended liquid crystal particles in the flow. While the presented technique is not entirely new, we have tried to present a clear concept of the technique and offer some novel ideas in solving various technical problems in measuring color through image processing techniques. Also, it has been our intention to make this paper relatively self-contained and to some degree a review paper. Thus, clarification of some basic conceptual ideas or definitions were necessary.

The paper is structured to review the concept of color measurement, the image capturing and processing techniques and finally presentation of the application of an integrated temperature measurement system to the problem of a heated vortex ring.

1.2 Properties of liquid crystal particles as temperature sensors

Since conventional visual information processes deal with data whose frequency lies within the visible range, it is important that the sensors indicating temperature changes do so by changing their reflective qualities in the visible range. Second, these sensors must be such that they do not alter the flow structure when placed in the flow and must therefore be quite small. Cholesteric liquid crystals, temperature sensors just recently implemented within the last two decades for applications to flow visualization, conveniently satisfy these criteria and were therefore chosen as the desired temperature sensors.

The cholesteric liquid crystal is composed of layers of liquid crystal sheets. However, in each sheet the molecules are aligned in a slightly different orientation with respect to their adjacent layers (Fig. 1). It is this property of the cholestric liquid crystal that is responsible for its color reflection behavior (Parsley 1987).

When unpolarized light hits the liquid crystal, it is split into two linear polarized components. Due to the anisotropy

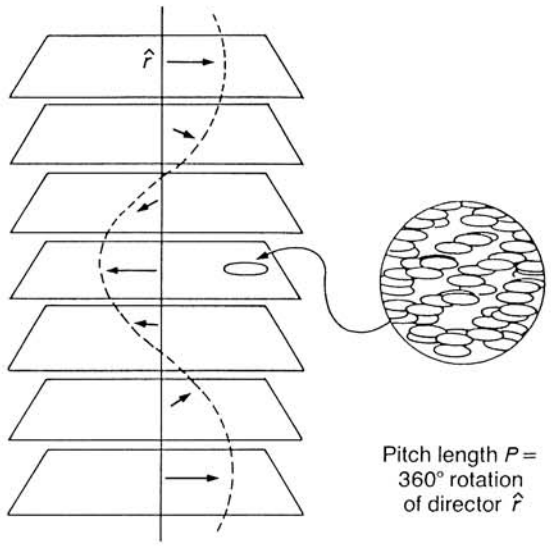

Fig. 1. The cholestric (chiral nematic) liquid crystal structure. The director (arrow) traces out a helical path within the medium. Reprinted with permission from Dr. Parsley at Hallcrest, 1820 Pickwick Lane, Glenview, Ill. 60025 USA

of the liquid crystal, the right-handed and the left-handed components of the polarized light each see a different refractive index, resulting in the rotation of the light's polarized plane. When the optical wavelength ($n\,p$) is equal to the wavelength of the incident light (h),

$$h = n\,p$$

where n is the average refractive index of the liquid crystal and p is the pitch, the circularly polarized light in the same rotational direction as the helix is reflected in a manner similar to Bragg X-ray reflection, while the circularly polarized light in the opposite direction is transmitted through the liquid crystal (Gray 1987).

As the temperature of the liquid crystal changes, the distance between the sheets of liquid crystal layers changes tending to increase the pitch, and the angular direction of each layer of liquid crystals increases with respect to its adjacent layers tending to decrease the pitch. The second effect dominates over the first, and as will be seen in the calibration curve, is highly non-linear with respect to temperature changes. Due to these effects, the color reflection of the liquid crystals is highly dependent upon the angle from which it is viewed with respect to the incident illumination. Thus, any changes in the viewing angle results in changes of perceived colors.

The pitch of the liquid crystal layers is not only sensitive to temperature, but also to shear stress and to magnetic fields as well. However, by encapsulating the liquid crystal, and using them in a non-magnetic environment, these effects can be eliminated. The liquid crystal is also prone to deterioration due to chemical reactions with reactants within the ambient fluid as well as radiation due to ultra-violet light. Reactions with reactants in the ambient fluid is prevented through encapsulation of the liquid crystal and deterioration is prevented by filtering out the ultra-violet components from all light sources illuminating the liquid crystals.

The temperature response time of the liquid crystals is an important consideration since a slow response time would result in erroneous temperature values. Since the liquid crystal fluid is encapsulated, the response time of both the liquid crystal and the encapsulating shell should be taken into account. Both of these effects can be taken into account by modelling the micro-encapsulated liquid crystal particle as a sphere of diameter d initially at temperature T_0, and the surrounding ambient fluid at temperature T_s. Dimensional analysis suggests two dimensionless parameters with a particular solution:

$$\frac{T_s - T_c}{T_s - T_0} = f\left(\frac{\alpha\, t}{d^2}\right)$$

where T_c is the transient temperature of the sphere at its center, t is the time, and alpha is the thermal diffusivity of the liquid crystal. The functional forms of the above relationship have been determined for different shapes by Williamson and Adams (1919). For a sphere,

$$\frac{T_s - T_c}{T_s - T_0} = 0 \quad \text{at} \quad \frac{\alpha\, t}{d^2} \cong 0.15$$

Thus, by seeding the flow of interest with the correctly-sized neutrally buoyant liquid crystals, we can avoid the problem of altering the flow, and at the same time have the particles follow the flow accurately and respond quickly.

1.3 Previous applications of liquid crystals

The application of liquid crystals to flow visualization is well known. Klein (1968) was the first to report the use of liquid crystals for flow visualization in wind-tunnel experiments. Klein applied an unencapsulated layer of liquid crystal solution to his test model, and was thus able to qualitatively study the steady-state boundary-layer temperature distributions of the model. Lemberg (1971) extended this work by using the same technique to visualize the unsteady boundary-layer on a model surface. Since the color play of the liquid crystal is sensitive to shear stress, the above techniques did not allow for accurate qualitative or quantitative temperature measurements. However, McElderry (1970) solved this problem by using encapsulated liquid crystals in an experimental technique similar to Klein's technique. Ogden and Hendricks (1984) further advanced this qualitative technique for surface analysis in water tunnels by using liquid crystals covered with a layer of acrylic polymer coating and a layer of polyurethane coating. This not only shielded the crystals from shear stresses but also prevented chemical contamina-

tion of the crystals by the water. Most recently, Rhee et al. (1984, 1986) expanded the use of encapsulated liquid crystals to study temperature fields in flow structures rather than on model surfaces. By mixing the encapsulated liquid crystals within the flow and illuminating a two-dimensional cross-section of the flow with a white sheet of light, the authors were able to study heated Taylor-Görtler-like longitudinal vortices. Color photographs showed pathlines, flow structures, and temperature distributions which otherwise would not have been deducible. Unfortunately, no methods were shown to extract quantitative results from the photographs. Finally, this flow visualization technique was also implemented by Bergman and Ungan (1988) to qualitatively assess the flow structure and temperature distribution of a double-diffusive convection in a two-layer, salt-stratified solution destabilized by lateral heating and cooling.

Efforts, have been made to quantify the temperature field through the use of liquid crystals. Cooper et al. (1975) used encapsulated liquid crystals to measure the variation of the Nusselt number on a circular cylinder placed in a crossflow of air. However, even through satisfactory results were obtained, the color play of the liquid crystal was calibrated against the human eye, and was therefore subject to human bias.

The human factor can be removed by capturing images of the liquid crystal's color reflections and calibrating the liquid crystals through image processing analyses for precise quantitative flow visualization. Measuring color, however, is not as easy as it may appear. The term "color" is not easily defined and in attempts to specify color, various color spaces have been created. Thus, a review of some of the spaces is necessary and will be discussed below.

1.4 Color space

The subject of color measurement, or calorimetry (Wright 1964; Wyzecki and Stiles 1982; MacAdam 1985; Agoston 1987), first started when it was noticed that certain colors could be matched by combining light from three monochromatic sources, called primaries, in correct proportional intensities. The matched color is then expressed in terms of three numbers representing the three sources of monochromatic light. A necessary requirement for selecting the three primaries was that when mixed in equal amounts, the color "white" should be reproduced. This implies that various combinations of the primaries produce different "whites", one of which must be chosen as the white reference. In a series of carefully done experiments, Wright (1928) using red (700 nm), green (546.1 nm), and blue (435.8 nm) as their three primary sources and an incandescent tungsten lamp (2,900 K color temperature) light as their white reference, found the values necessary to duplicate the domain of almost all colors. These values formed the color-matching functions which were then used to calculate the tristimulus values, red, green, and blue. To quantify the color characteristics observed, the color-matching functions were then used to calculate the tristimulus values, R, G, and B through the Eq.:

$$R = \int_{380}^{780} R_\lambda P_\lambda r_\lambda$$

$$G = \int_{380}^{780} R_\lambda P_\lambda g_\lambda$$

$$B = \int_{380}^{780} R_\lambda P_\lambda b_\lambda$$

where R_λ is the spectral reflectance of an object, P_λ is the spectral power of the light source, and r_λ, g_ρ and b_λ are the color-matching functions. The color spectrum can also be represented by their chromaticities where the chromaticities of a color are defined as:

$$r = R/(R+G+B)$$

$$b = B/(R+G+B)$$

$$g = G/(R+G+B)$$

where $r+g+b=1$. By convention, a chromaticity diagram has been defined using the r and g values only. In 1931, these tristimulus values became internationally accepted as the CIE (International Commission on Illumination) tristimulus values for the spectral primary RGB system. A complication in Guild's and Wright's RGB color system, was that negative amounts of primaries were required to match certain colors. A negative amount of a primary is obtained by adding that primary to the desired reproducible color rather than to the other primaries. Due to practical reasons, it was decided by the CIE to make a system where only positive amounts of primaries exit. Thus a set of primaries (XYZ) came into existence through the linear transformation:

$$\begin{bmatrix} X \\ Y \\ Z \end{bmatrix} = \begin{bmatrix} 0.49 & 0.31 & 0.2 \\ 0.177 & 0.813 & 0.011 \\ 0.0 & 0.01 & 0.99 \end{bmatrix} \begin{bmatrix} R \\ G \\ B \end{bmatrix}$$

Unfortunately, the CIE XYZ color system did not represent equal color differences by equal distances. The uniform chromaticity scale (UCS) system (Y, u, v) remedies this drawback by transforming the ellipses with large eccentricities into ellipses with small and more uniform eccentricities through the transformation:

$$u = 4X/(X+15Y+3Z)$$

$$v = 6Y/(X+15Y+3Z).$$

$$Y = Y$$

Upon the advent of the color television, the National Television System Committee (NTSC) transmission system developed the (YIQ) system. This system is capable of transmitting color images using the existing monochromatic television system without increasing the bandwidth requirement.

Another perspective is based upon the perceptual attributes of color: hue, saturation, and intensity. Hue refers to the essence of the color; i.e., on whether the color is red, or green, and so forth. Put more specifically, different hues correspond to different wavelengths. Saturation refers to how much white is mixed with a particular hue. For example, if a color is pure red, then it is unsaturated, but if it is mixed with white and the resultant color is pink, then there is a certain percent of saturation involved depending on how pink the color is. Intensity refers to the level of brightness of the color. The saturation and the hue both determine the "quality" of the order, and are referred to as the chrominance of the color, whereas the intensity determines the quantity of the color, and is therefore referred to as the luminance of the color. Any of the color models above can be represented in the *HSI* format. For example, the *HSI* representation of the *Y u v* space can be obtained through the transformation

$$H = \tan^{-1}(V^*/U^*) \qquad 0 < H < 2^* pi$$

$$S = [U^{*2} + V^{*2}]^{1/2}$$

$$W^* = 25(100\ Y)^{1/3} - 17 \qquad 1 < 100\ Y < 100$$

where $U^* = 13\ W^*(u - u_0)$, $V^* = 13\ W^*(v - v_0)$, and u_0, v_0 are chromaticity coordinates of the white reference in the *Y u v* space. The *HSI* representation of the *RGB* color space is obtained through the transformation

$$\begin{bmatrix} v_1 \\ v_2 \\ I \end{bmatrix} = \begin{bmatrix} 2/\sqrt{6} & -1/\sqrt{6} & -1/\sqrt{6} \\ 0 & 1/\sqrt{6} & -1/\sqrt{6} \\ 1/3 & 1/3 & 1/3 \end{bmatrix}$$

$$H = \tan^{-1}(v_1/v_2)$$

$$S = (v_1^2 + v_1^2)^{1/2}$$

Note that the graphical representation of the *HSI* and *RGB* spaces shown simultaneously in Fig. 2 indicates that the *HSI* space is essentially a cylindrical coordinate representation of the *RGB* space.

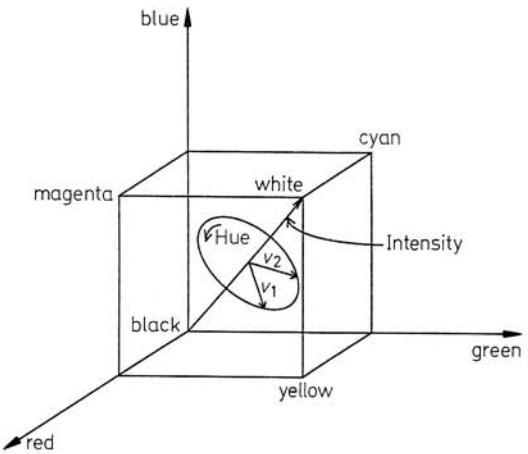

Fig. 2. The *RGB* and the *HSI* color space shown simultaneously indicates that the *HSI* color space is a cylindrical coordinate representation of the *RGB* color space

A feasible color system must be selected to do the analysis of the liquid crystal color reflection. Calibrating and analyzing images in the *RGB* and *XYZ* CIE color space is not computationally appropriate since processing of all three components are necessary to produce the spectral content of the image. For example, Wilcox et al. (1985), digitizing color photographs of constant temperature fields, and Akino et al. (1988), digitizing images directly, calculated transmittance values for each of the red, green, and blue primaries. The method proved to be numerically cumbersome, since investigations showed that all three transmittance values were necessary to calibrate temperature. Working in the *Y u v* and the *YIQ* system is also not computationally appropriate as the spectral content of an image is stored jointly within the *u*, and *v*, and the *I*, and *Q* coordinates, respectively.

Further calibration approaches were investigated using the *HSI* format. In the same paper, Akino et al., (1988) also calibrated the temperature with hue in the *RGB* space, the *XYZ* space, and the *u v Y* space. Due to the behavior of the liquid crystals used, the calibration curves showed three regions of very low sensitivity to temperature, and it was thus concluded that the linear multiple regression model described earlier was the optimum choice for calibration. Despite their results and the different response of their liquid crystals, the most beneficial color system found by the present authors is the *HSI* representation of the *RGB* color space. Within this system, the hue content and the intensity content of an image are already separate and independent of one another, thus allowing for fast and effective data acquisition and analysis.

2 Image capturing technique and experimental set-up

Several attempts have been made to calibrate liquid crystals via computers so that the human bias could be removed. Wilcox et al. (1985), mentioned earlier, digitized color photographs and used three interference filters to separate the primaries in an effort to remove the human factor. By doing so, they created the added work of calibrating each roll of film since each roll was slightly different from the others used. Furthermore, once the film was calibrated, three separate digitization of the same image, each filtered through a different interference filter, was required to calibrate the liquid crystals. Instead of using three separate interference filters to define a color space, Hiller and Kowalewski (1987) used narrowband interference filters to calibrate the liquid crystals. Akino et al. (1988) by-passed color photography, and captured images directly onto their image-processing system. However, it was still necessary to digitize each of their images three times through the interference filters, since they used a single-chip CCD camera. Finally, Hirsch et al. (1988) using a color camera captured images onto their image processing system. By transforming their color space from *RGB* into *Yuv* space, they were able to analyze the colors by only using the *u* and *v* components, and thus

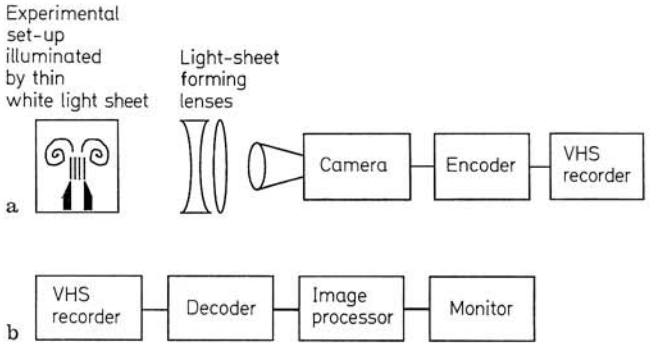

Fig. 3. a Block diagram showing equipment set-up for collecting data for both calibration and the experiment; **b** block diagram showing equipment set-up for retrieving and analyzing the data for both the calibration and the experiment

reduce their workload when compared with their predecessors.

In the present experiment, the authors side-stepped the use of interference filters by capturing images through a three-chip color camera directly into *RGB* space. The *RGB* signals are inputted into the IBM/AT based image processing boards, and translated into *HSI* space for analysis (Fig. 3a–b). This gives the advantage of using only one component of the *HSI* space, the hue, to describe the color reflections from the liquid crystal particles. Moreover, images were recorded onto super-VHS video via an *RGB*/NTSC encoder at 30 frames per second to allow for analyses of time-dependent flows. The images from video are then played back and decoded into *RGB* via a NTSC/*RGB* decoder. The encoders and decoders used in this experiment are specially designed to eliminate all losses of information associated with standard encoders and decoders when processing *RGB* signals into NTSC signals and vis versa. The physical dimensions corresponding to each of the captured images is 11.2 cm by 16.3 cm. Due to the rectangular shape of the pixels, each pixel therefore resolved a horizontal distance of 318 μm and a vertical distance of 234 μm. Finally, selected areas of interest within the images where chosen, and raw data are collected and analyzed. Each of the hue, saturation, and intensity values range from 0 to 255. In all measurements, acceptable hue values are chosen by thresholding their corresponding intensity values.

It was decided to test this novel temperature measuring approach to the problem of heat transfer in an unsteady heated vortex-ring travelling through a colder ambient. A description of the calibration and the experimental set-up is given below before discussing results.

2.1 Calibration set-up and procedure

A 12.7 cm by 12.7 cm by 25.4 cm pyrex tank is filled with a water/liquid crystal mixture. The liquid crystals used are 150 micro-meters in diameter, reflecting red at ~23 °C, and reflecting blue at ~26 °C. The mean nearest distance between liquid crystal particles is 4 pixels or assuming a mean distance of 277 μm per pixel, approx. 1.1 mm. The thermal diffusivity of these liquid crystals if $5.8 \cdot 10^{-8}$ m^2/s, corresponding to a time response of ~0.06 seconds. A Xenon short-arc lamp and a series of optics are used to create a sheet of white light 3 mm thick in order to illuminate a two-dimensional section of the mixture with an incident light whose spectrum is flat across the visible wavelengths (Fig. 3a–b). If the illuminated liquid crystal particles are not in their color-reflecting temperature range, their encapsulating shell scatters white light, where the hue value is not a correct temperature measurement. Therefore, it is imperative for the liquid crystal particles to be in a temperature environment that corresponds to their color-reflecting temperature range. The camera is located such that the calibration set-up is viewed by the camera through a maximum angle of 9.7 degrees. The mixture is then heated to different constant temperatures, where for each temperature images are captured and hue values are recorded. A fifth order polynomial is used to fit a calibration curve through the collected points. Using the thresholding condition, the hue values are collected from the calibration images, and averaged. The hue averages are then plotted against their corresponding temperature, and a fifth order polynomial is used to curve fit the data. In order to account for angular color variations within the image, local sections of 64 by 64 pixels are chosen from the calibration images, and local calibration curves are obtained. A typical local calibration curve is shown in Fig. 4. The calibration polynomial has the form:

$$T = 21.943 + 0.04179 \cdot H - 1.1346\, e-3 \cdot H^2 + 1.4657\, e - 5 \cdot H^3 - 8.0335\, e-8 \cdot H^4 + 1.5912\, e-10 \cdot H^5$$

$$R = 1$$

where H is the hue value, T is the temperature, and R is the correlation coefficient. The red corresponds to a hue value of 56, and the blue corresponds to a hue value of 220. Since the calibration curve is non-linear, the temperature resolution ranges from a minimum of 0.01 °C at 22.73 °C to a maximum of 0.12 °C at 26.09 °C (Fig. 4).

2.2 Experimental set-up and procedure

The experimental set-up is composed of two parts. The first part consists of a constant pressure piston tube with an internal diameter of 2.06 cm. The piston is controlled through a timing device, and pushes fluid from the tube into a pyrex tank filled with a water/liquid crystal mixture at ~23 °C. The second part consists of a heated mixture of water and liquid crystal particles which is used to fill the piston with a mixture at ~26 °C upon shooting the vortex-ring (Fig. 5). To compensate for the density differences of the hotter and less dense vortex-ring travelling through the colder and heavier ambient, salt was added to the vortex-ring solution to minimize buoyancy effects felt by the vortex ring. The Xenon light sheet described in the previous section

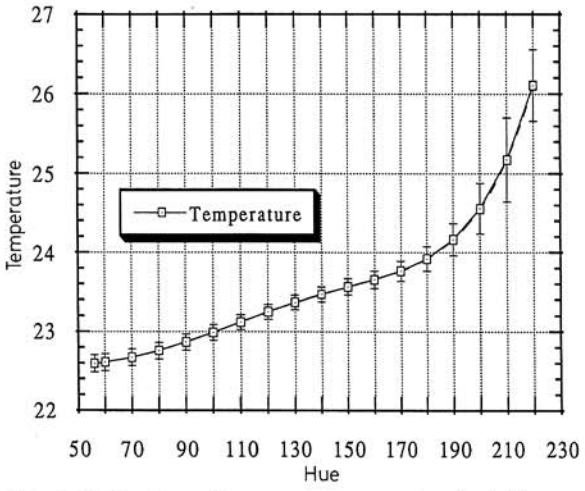

Fig. 4. Calibration of temperature versus hue including error bars after taking into account the finite viewing angle of the camera

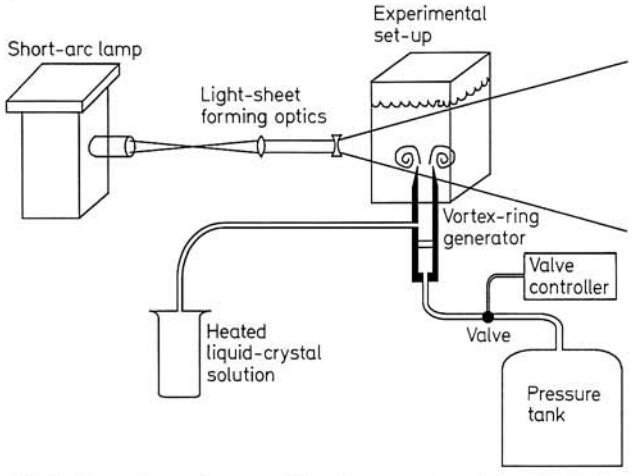

Fig. 5. Experimental set-up. The short-arc lamp is used to create a light-sheet that disects the vortex-ring along its diameter. A heated liquid-crystal solution is used to fill the tube generator with heated fluid and the pressure tank is used to generate the vortex-ring

is needed to illuminate the vortex-ring along its axis of symmetry. The vortex-ring is then generated by the tube and the light source is used to illuminate its axis of symmetry. After an initial rise time of ~0.1 seconds, the velocity of the piston reached a constant value of ~4.95 cm/s, corresponding to a Reynolds number of ~1,022 based on the diameter of the vortex-ring generator. Finally, the image-processing system is used to capture the image via the 3-chip camera in the *HSI* color space. The location of the 3-chip color camera from the experiment is such that the same viewing angle of the calibration is duplicated. The hue field is then translated into temperature through the calibration curve and analyzed.

3 Data analysis

Hue values of the images captured directly from the camera were chosen and stored by thresholding their intensity values. Fig. 6 is an example of a typical image of the vortex-ring captured directly with the color camera. Fig. 7 shows the resulting processed images of the vortex-ring. Black areas indicate areas where no data exists or are below the intensity threshold level. The stored hue values were then translated into temperature through the calibration curve. A Gaussian window was chosen to interpolate the non-uniformly distributed data and a 12 by 12 pixel window was used to smooth the data (Agui and Jimenez 1987, Rignot and Spedding 1988). The corresponding contour plot and smoothed surface plot of the above images are shown in Figures 8a–b. As can be seen from each of the figures, the center of the vortex-ring is at a higher temperature with respect to the ambient fluid. The higher temperature fluid continues through the center of the vortex-ring, circles around the outer edge of the vortex-ring, and in doing so, engulfs a pool of cooler fluid, thus producing the cores of the vortex-ring. It is important to note that the edges of the vortex-ring always remain at a higher temperature. An order of magnitude calculation shows the diffusion time to be

$$\tau_1 \cong \frac{L^2}{\alpha} \cong \frac{1\ \text{cm}^2}{0.01\ \text{cm}^2/\text{s}} = 100\ \text{s}$$

while an eddy turnover time to be

$$\tau_2 \cong \frac{L}{u} \cong \frac{1\ \text{cm}}{5\ \text{cm}} = 0.2\ \text{s}$$

where L is the diameter and the characteristic length scale for the vortex-ring, α is the thermal diffusivity of water, and u is the characteristic velocity of the vortex-ring. Since the eddy turnover time is less than the diffusion time by 3 orders of magnitude, the edges of the vortex-ring do not have time to diffuse with the ambient fluid. Note that these times are longer than the response time of the liquid crystal by at least an order of magnitude, thus allowing for instantaneous temperature response.

To demonstrate the use of this technique for analyzing time-dependent flows, the temperature profiles of the centerline of the vortex-ring are shown at various stages of its development in Figures 9a–e. It is interesting to note that the vortex-ring's initial temperature profile is flat, simulating a step-function. However, in time, the centerline temperature

Fig. 6. Example of a vortex-ring initially developing

Fig. 7. Initially developing vortex-ring image after being processed

Fig. 8. **a** Contour plot of Figs. 7 and 8. Each contour represents a temperature increment of 0.25 °C with the lowest temperature at 22.6 °C shown by red, and the highest temperature at 25.5 °C shown by dark blue; **b** surface pot of Fig. 8a

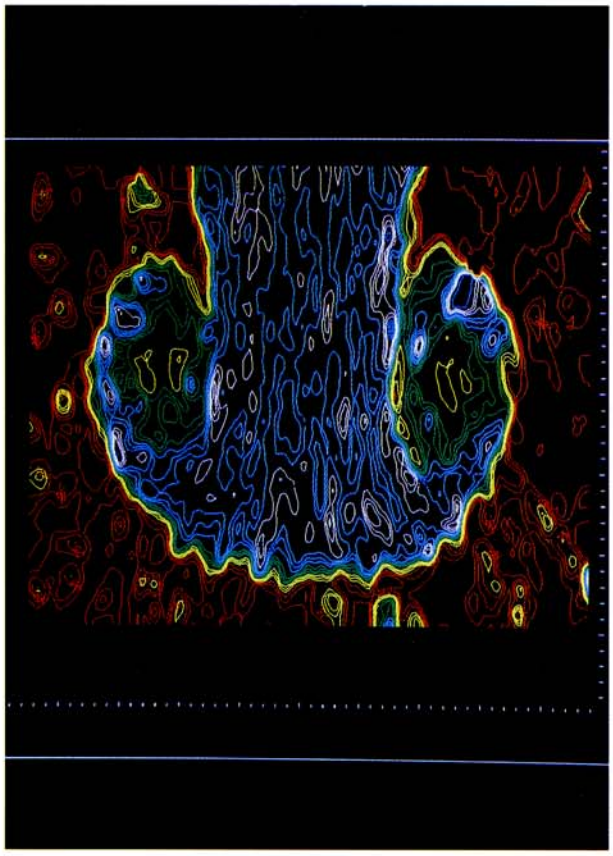

a

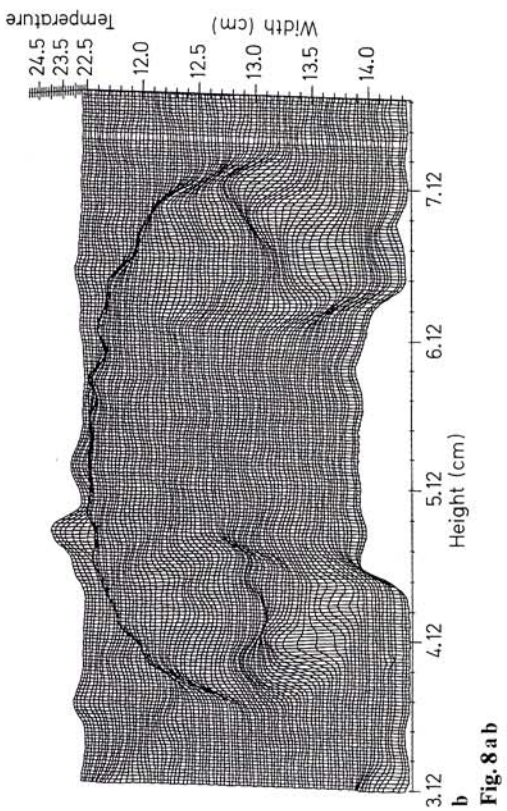

b

Fig. 8 a b

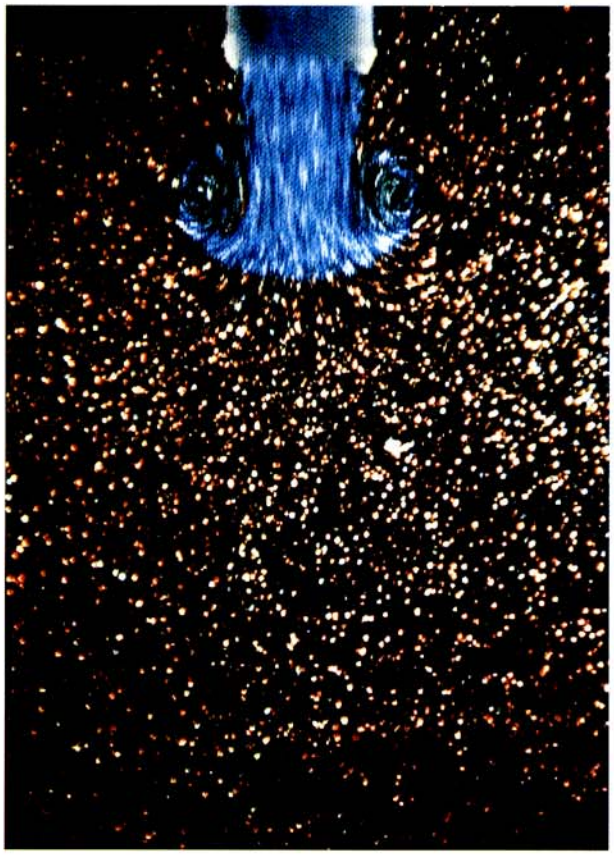

Fig. 6

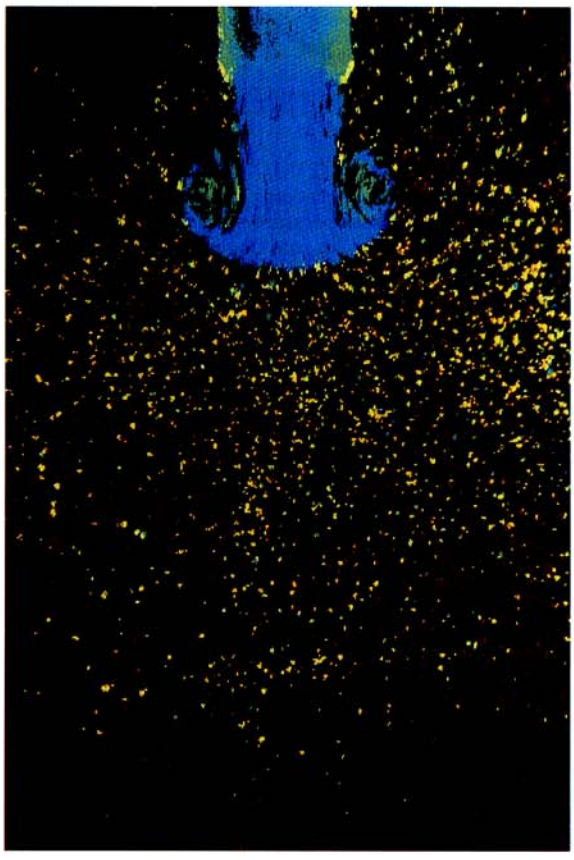

Fig. 7

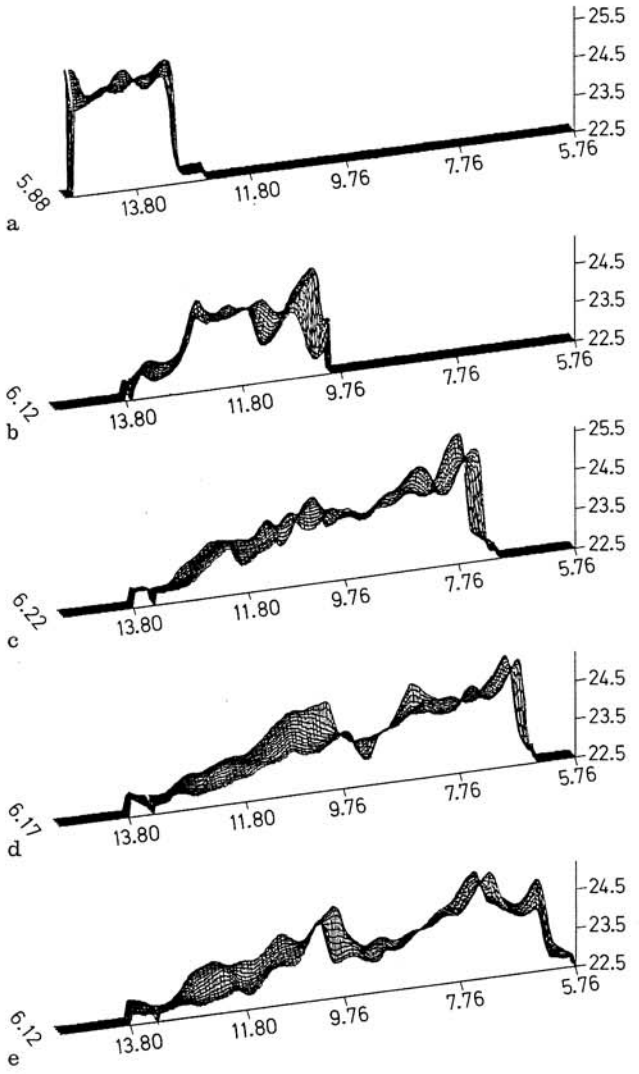

Fig. 9. **a** Temperature profile of the vortex-ring's centerline when its cores are 0.7 cm from the nozzle; **b** temperature profile of the vortex-ring's centerline when its cores are 3 cm from the nozzle; **c** temperature profile of the vortex-ring's centerline when its cores are 5.9 cm from the nozzle; **d** temperature profile of the vortex-ring's centerline when its cores are 6.6 cm from the nozzle; **e** temperature profile of the vortex-ring's centerline when its cores are 7.3 cm from the nozzle

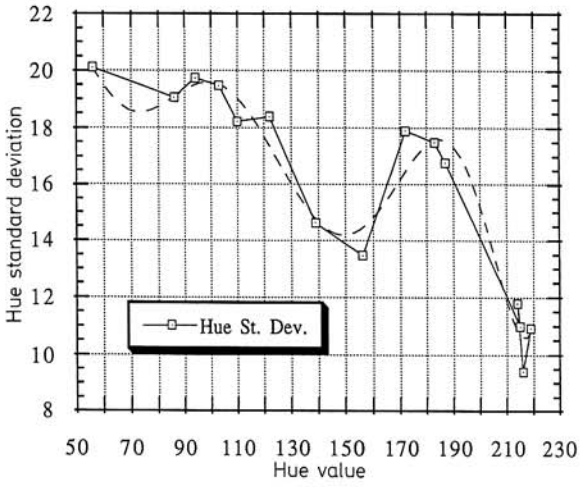

Fig. 10. Standard deviation of the hue versus values

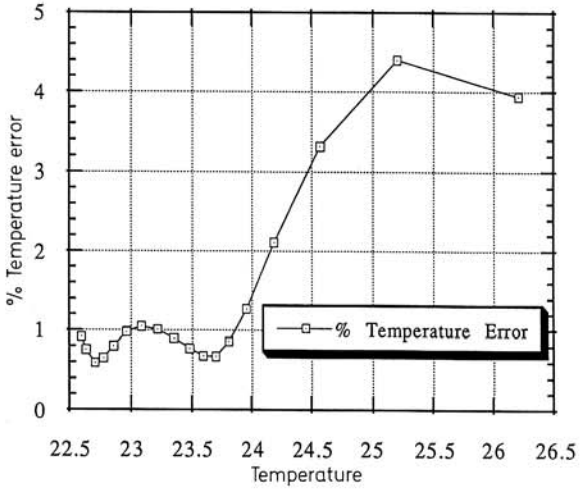

Fig. 11. Percent temperature error versus temperature

profile looses its step-function-like characteristic, eventually decaying linearly from its sharp high temperature front.

4 Error analysis

There are two sources contributing to the uncertainty in the temperature measurements. The first involves an error in the calibration and the second involves an uncertainty in the interpolation scheme.

4.1 Calibration

Constant-temperature images (512 by 480 pixels) were used to calibrate the liquid crystal particle's temperature. The standard deviation of the hue values used to calibrate the liquid crystal particles, and the fifth order polynomial fit to these points are shown in Fig. 10. Note that the lower values of the hue corresponding to the red produce the higher hue standard deviations. Fig. 11 shows the percent temperature error at each temperature resulting from the hue standard deviations. Note that at lower temperatures, the temperature standard deviation is lower than the temperature standard deviation at higher temperatures, contrary to the hue standard deviation behavior shown in Fig. 10. At lower temperatures, the lower slope of the calibration curve affected by the higher hue standard deviation produces a small temperature standard deviation. Likewise, at higher temperatures, the higher slope of the calibration curve converts the lower hue standard deviations into higher temperature standard deviations. Also, note that the percentage temperature error for the calibration is less than 5%. Fig. 12 shows the calibration curve again including error bars mostly due to angular variations within each of the images. In order to reduce the

standard deviations due to angular variations, areas of 64 by 64 pixels were averaged from each constant-temperature images. This area corresponds to a maximum viewing angle of 1.5 degrees. Fig. 4 shows that these standard deviations are highly reduced when these angular variations are taken into account.

4.2 *Interpolation*

Since the travelling vortex-ring is a transient process, every interpolated node of each image is a single measurement. Thus, we do not have the luxury of multiple measurements for every node of each image to produce a statistical data base. The solution is, for each image of M points, randomly pick M number of data points, repeating some and skipping others, and from them interpolate a temperature field. Doing this process several times for the same image creates an ensemble of temperature fields, thus forming the statistical data base. Temperature values at every node of each image are statistically analyzed and uncertainty values are calculated at each node. This technique eventually became known as the "bootstrapping" technique. Agui and Jimenez (1987) applied the bootstrapping technique by calculating the bootstrapping erros directly from the particle values. Rignot and Spedding (1988) modified the approach by first interpolating the field directly from the particles, and then calculating the bootstrapping error from this interpolated temperature field. The authors showed that the important parameters in determining the root mean squared error (RMSE) are

$$\text{RMSE} = f\,(L/h,\ h/d)$$

where L is the characteristic length scale of the flow, d is the mean nearest neighbor distance between samples, and h is a free parameter in the Gaussian window interpolation. The parameter d can be approximated by

$$d = [1/(\Pi \cdot n)]^{1/2}$$

where n is the average number of particles per area. By generating an artificial pure vortex flow, Rignot and Spedding calculated both true errors and bootstrapping errors for the purpose of comparison. They concluded that even though the distributions and comparative error levels are accurate, the absolute error may be in doubt by up to 100 percent. However, they also state that for the ranges of h/d and L/h observed, the true error is approximately twice as large as the bootstrapping error.

The bootstrapping technique used by Rignot and Spedding was implemented in estimating the uncertainty in the interpolation of the temperature field of the vortex-ring. The factor of two mentioned above is also included to estimate

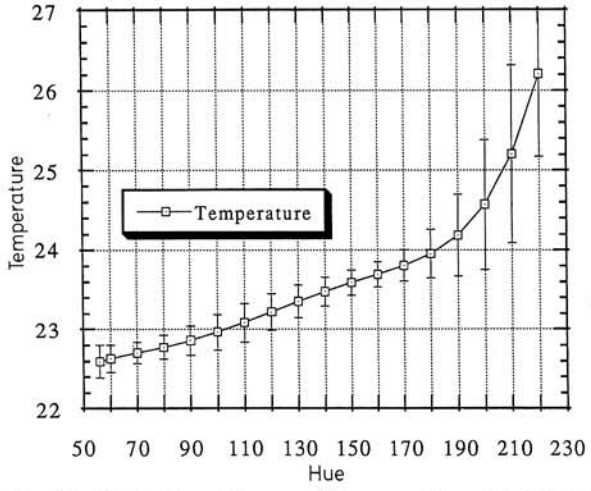

Fig. 12. Calibration of temperature versus hue with error bars resulting from the whole image analysis

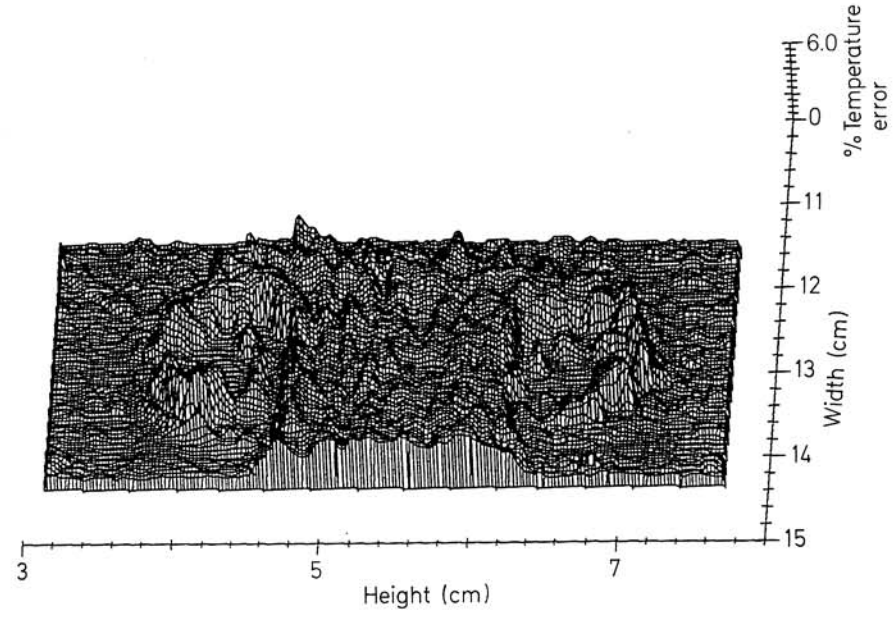

Fig. 13. Percent temperature error distribution of the initially developing vortex-ring (Figs. 6–8)

the true interpolation error from the bootstrapping error. Since the interpolation error and the calibration error are independent, the square root of the sum of the squares of these errors is calculated to give the total temperature error. Fig. 13 shows the percent temperature error for the temperature fields corresponding to Fig. 8 b. The maximum temperature error in Fig. 13 is calculated to be 4.81%, while its average temperature error is calculated to be 1.32%. Thus, it can be concluded that the temperature uncertainties estimated are therefore accurate and within reason.

5 Conclusion and recommendations

A new approach for quantifying temperature in two-dimensional flow fields is thus introduced and demonstrated for a heated vortex-ring. The errors of the results are shown to be within 5 percent of the temperature field. As can be seen in Fig. 12, the temperature standard deviations are rather large when whole images are used to calibrate the liqid crystals, because the hue standard deviations include slight color variations resulting from the finite angle viewed by the camera. However, Fig. 5 shows this error to be greatly reduced if the finite viewing angle is taken into account. Presently, work is being done to improve the calibration method to minimize these standard deviations even further. It is also recommended to use smaller particles in order to obtain a better response time from the liquid crystal particles.

Acknowledgements

This work is sponsored by the Defense Advanced Research Project Agency – ACMP through the URI program under contract number DARPA/ACMP N00014-86-k-0758. The authors would like to thank Mr. Alex Weigand for his assistance in the heated vortex-ring experiment.

References

Agoston, G. A. 1987: Colour theory and its application in art. Berlin, Heidelberg, New York: Springer

Agui, J. C.; Jimenez, J. 1987: On the performance of particle tracking. J. Fluid Mech. 185, 447–468

Akino, N.; Kunugi, T.; Ueda, M.; Kurosawa, A. 1988: Liquid crystal thermometry based on automatic color evaluation and applications to measure turbulent heat transfer. Transport Phenomena in Turbulent Flows, 807–820

Bergman, T. L.; Ungan, A. 1988: A note on lateral heating in a double-diffusive system. J. Fluid Mech. 194, 175–186

Cooper, T. E.; Field, R. J.; Meyer, J. F. 1975: Liquid crystal thermography and its application to the study of convective heat transfer. J Heat Transfer 92, 442–450

Gray, G. W. 1987: Thermotropic liquid crystals. New York: Wiley

Hiller, W. J.; Kowalewski, T. A. 1987: Simultaneous measurement of temperature and velocity fields in thermal convective flows. Flow Visualization IV (Ed. Véret, C.) 617–622. Washington: Hemisphere

Hirsch, C.; Platzer, K. H.; Metzger, D. E.; Wittig, S. 1988: Instationäre Wärmeübergangsmessung unter Nutzung von thermochromen Flüssigkristallen als Temperaturindikatoren. 2D-Meßtechnik, DGLR-Bericht 88-04, 211–221

Klein, E. J. 1968: Application of liquid crystal to boundary layer flow visualization. AIAA Paper No. 68–376

Lemberg, R. 1971: Liquid crystals for the visualization of unsteady boundary layers. Third Canadian Congress of Applied Mechanics: Calgary

MacAdam, D. L. 1985: Colour measurement: Theme and variations. Berlin, Heidelberg, New York, Tokyo: Springer

McElderry, E. D. 1970: Boundary layer transition at supersonic speeds measured by liquid crystals. Air Force Flight Dynamics Laboratory. FDMG TM 70-3

Ogden, T. R.; Hendricks, E. W. 1984: Liquid crystal thermography in water tunnels. Exp. Fluids 2, 65–66

Parsley, M. 1987: An introduction to thermochromic liquid crystal products. Illinois: Hallcrest

Rhee, H. S.; Koseff, J. R.; Street, R. L. 1984: Flow visualization of a recirculating flow by rheoscopic liquid and liquid crystal techniques. Exp. Fluids 2, 57–64

Rhee, H. S.; Koseff, J. R.; Street, R. L. 1986: Simultaneous flow and temperature field visualization in a mixed convection flow. Flow Visualization IV (Ed. Véret, C.) 659–664, Washington: Hemisphere

Rignot, E. J. M.; Spedding, G. R. 1988: Performance analysis of automatic image processing and grid interpolation techniques for fluid flows. USC Aerospace Engineering Internal Report

Wilcox, N. A.; Watson, A. T.; Tatterson, G. B. 1985: Color/Temperature calibrations for temperature sensitive tracer particles. International Symposium on Physical and Numerical Flow Visualization, June 24–26, 65–74

Williamson, E. D.; Adams, L. H. 1919: Temperature distribution in solids during heating or cooling. Phys. Rev. 14, 99–114

Wright, W. D. 1964: The measurement of colour. Princeton: Van Nostrand

Wright, W. D. 1928: A re-determination of the trichromatic coefficients of the spectral colours. Trans. Opt. Soc. 30, 141

Wyszecki, G.; Stiles, W. L. 1982: Color science: concepts and methods, quantitative data and formulae. New York: Wiley

Received July 1, 1990